One-dimensional Self-assembly of Metal-Organic Octahedra towards Mechanically Flexible Microporous Aerogels

Ayana Miyata,[1,2] Shun Tokuda,[1,2] Masataka Yamashita,[3] Mako Kuzumoto,[3] Takuma Aoyama,[3] Taichi Nishiguchi,[4] Masaki Negoro,[4] Guan-Sian Lee,[5] Brian R. Pauw,[6] Glen J. Smales,[6] Yi-Tsu Chan,[5] Kazuyoshi Kanamori,[4] Tomoko Inose,[1,2] Kenji Urayama,[3] Kunihisa Sugimoto,[7] Shuhei Furukawa[1,2,*]

[1]Institute for Integrated Cell-Material Science (WPI-iCeMS), Kyoto University, Yoshida, Sakyo-ku, Kyoto 606-8501, Japan.

[2]Department of Synthetic Chemistry and Biological Chemistry, Graduate School of Engineering, Kyoto University, Katsura, Nishikyo-ku, Kyoto 615-8510, Japan.

[3]Department of Material Chemistry, Graduate School of Engineering, Kyoto University, Katsura, Nishikyo-ku, Kyoto 615-8510, Japan.

[4]Department of Chemistry, Graduate School of Science, Kyoto University, Kitashirakawa, Sakyo-ku, Kyoto 606-8502, Japan.

[5]Department of Chemistry, National Taiwan University, Taipei 10617, Taiwan.

[6]Federal Institute for Materials Research and Testing (BAM), Unter den Eichen 87, 12205 Berlin, Germany.

[7]Department of Science, Faculty of Science and Engineering, Kindai University, Kowakae, Higashiosaka, Osaka 577-8502, Japan.

ABSTRACT:

INTRODUCTION

The mechanical properties of materials intrinsically depend on the connectivity of their building blocks. A classic example is the difference between diamond and its low-dimensional allotropes, such as graphene and carbon nanotubes (CNTs). Diamond possesses a three-dimensional (3D) sp^3 covalent network of carbon atoms, which provides significant stiffness.[1,2] Due to the difficulty of the dislocation, diamond lacks plastic deformability, exhibits little capacity for stress dissipation, and consequently fractures when the applied stress exceeds a critical threshold.[3] In contrast, graphene[4,5] and CNTs[6,7] are composed of sp^2 bonding networks of carbon atoms, forming two-dimensional (2D) sheets and one-dimensional (1D) tubular structures, respectively. Such topological anisotropy allows them to deform flexibly in response to applied stress. Thus, the dimensionality reduction of the bonding network increases the degrees of freedom for stress dissipation.[8]

A similar concept can be applied beyond covalent linkages to molecular assemblies constructed through non-covalent interactions. Dense packing of organic molecules by non-covalent interactions forms molecular crystals with rigid yet brittle mechanical properties.[9] Recent studies have shown that the control of the anisotropy of molecular arrangements within a crystal offers a new flexibility with directional deformation, so-called bending crystals.[10] Ultimate reduction of the dimensionality of molecular assemblies through non-covalent interaction provides 1D supramolecular polymers. Thanks to their fibrous structures self-assembled from pre-designed molecules, supramolecular polymers often exhibit notable mechanical flexibility.[11] Large biological materials also follow a similar trend. For instance, proteins as large macromolecules can be assembled into 3D periodic lattices and form brittle crystals.[12] When proteins are assembled into fibrous structures like spider silk, they exhibit remarkable mechanical properties suitable for various practical applications.[13]

Bridging the gap between small molecules and proteins, supramolecules have recently emerged as one of the essential building blocks for constructing superstructures. Supramolecules assembled from multiple molecular components typically range in size from 1 to 10 nm,[14] leading to the emergence of collective functions that are inaccessible to individual molecules alone.[15] Metal–organic polyhedra (MOPs) are one of the representatives of supramolecules, which exhibit defined polyhedral shapes and an intrinsic cavity.[16–18] Connecting MOPs to form solids via various bonding modes, including coordination or covalent bonds, provides a new porous material platform.[19–23] Very recently, we demonstrated that packing of MOPs solely with van der Waals interactions generates a series of 3D diamond frameworks with high stability and porosity, consequently as rigid microporous crystals of van der Waals

open frameworks: WaaFs.[24] Similar to the above mentioned connectivity of atoms, molecules and proteins, the dimensionality control of supramolecular assembly can lead to a new material system with controllable mechanical properties; however, most of the reported MOP assemblies are limited to 3D networks with poor mechanical flexibility. This is mainly because MOPs are often synthesized with isotropic geometries, and thus, the dimensional reduction of their assemblies has been challenging.

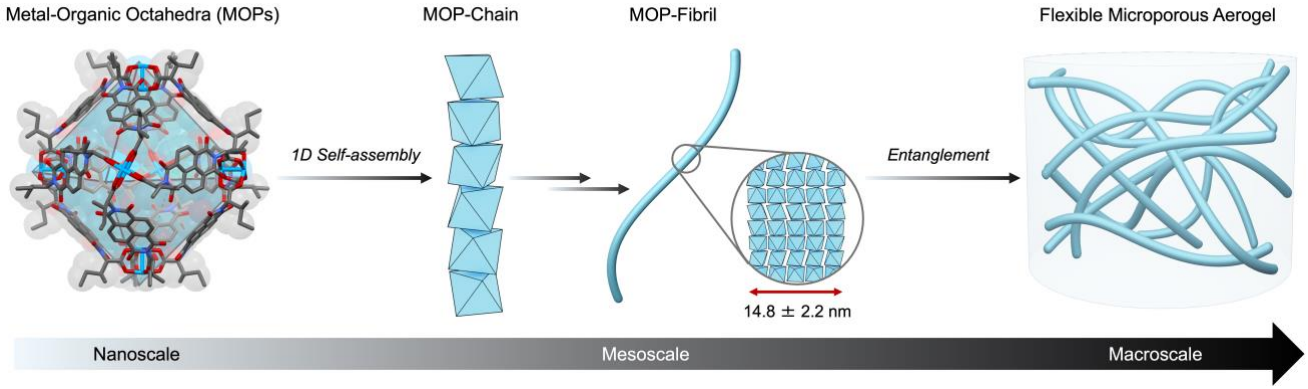

Figure 1. Schematic illustration of the one-dimensional (1D) self-assemblies of octahedral MOPs into mechanically flexible microporous aerogel through supramolecular polymerization.

Here we report the 1D self-assembly of octahedral MOPs through supramolecular polymerization, which leads to the formation of microporous aerogels with exceptional mechanical deformability (Figure 1). To achieve such supramolecular polymerization using MOPs as monomers, we tuned solvent conditions and found that poor solvents with high polarity and strong dispersive interaction induced the MOP-MOP interaction to form 1D fibrils, followed by a self-supporting gel. Through the supercritical CO_2 drying process, the resulting gels were converted to the corresponding aerogels. Gas adsorption measurements demonstrated that these aerogels possess uniform microporosity, originating from the intrinsic pores of MOPs. Throughout the uniaxial compression tests, the aerogel withstood up to 87% compressive strain without fracturing, demonstrating its high mechanical deformability. This result opens a venue for tuning the mechanical properties of supramolecular materials through the dimensional control of their assemblies.

RESULTS AND DISCUSSION

One-dimensional self-assembly of MOPs. Supramolecular polymerization is driven by non-covalent interactions between building blocks. To construct desired assemblies using such non-directional interactions, the structure of each building block should be rationally designed to facilitate efficient intermolecular interactions. Here, we selected a copper-based octahedral MOP molecule with a naphthalenediimide derivative linker, $[Cu_{12}(NDI\text{-}X)_{12}]$ (NDI-X = naphthalenediimide (NDI) dicarboxylate derivatives, where X represents amino acid codes).[24–26] This MOP possesses twelve NDI-X linkers and six Cu(II) paddlewheel moieties at its edges and vertices, respectively. One significant structural feature of this MOP family is the large facets of the octahedron composed of the three NDI π-conjugated planes oriented outward. Indeed, NDI-based planar π-conjugated cores are commonly employed in supramolecular polymers as building blocks to drive one-dimensional self-assembly.[27] Another characteristic feature is the structural versatility of the NDI-X linker. The NDI-X linkers are synthesized via a condensation reaction between 1,4,5,8-naphthalene tetracarboxylic dianhydride and an α-amino acid (X). By simply varying the α-amino acid used in this condensation reaction, diverse surface functionalities can be introduced, allowing fine-tuning of intermolecular interactions.

After screening various α-amino acids employed in the NDI-X linkers, we identified two promising candidates for supramolecular polymerization: MOP based on L-isoleucine (Ile) with a composition of $[Cu_{12}(NDI\text{-}Ile)_{12}]$ (**MOP-Ile**)[25] and MOP based on L-cyclohexyl glycine (Chg) with a composition of $[Cu_{12}(NDI\text{-}Chg)_{12}]$ (**MOP-Chg**), respectively (Figure 2). These MOPs were obtained as greenish-blue crystals by reacting copper(II) nitrate with the corresponding NDI-X linker (**Pristine-Ile** for **MOP-Ile** and **Pristine-Chg** for **MOP-Chg**) (Figure S1). Single-crystal X-ray diffraction (SC-XRD) analysis on these crystals confirmed the formation of the octahedral structure for both **MOP-Ile** and **MOP-Chg** (Figure S2). **Pristine-Ile** belongs to the space group $F432$, in which **MOP-Ile** molecules contact through their amino acid side chains, with their NDI planes facing each other. This corresponds to an edge-to-edge interaction between neighboring octahedra, and the shortest C···C distance was 4.28 Å (Figure S3 and Table S1). **Pristine-Chg** crystallizes in the space group $P2_1$, in which **MOP-Chg** contact with each other through crossed edge-to-edge interaction at the Chg moiety,

leading to a distorted FCC packing (Figure S4 and Table S2). The shortest C···C distance was 4.07 Å.

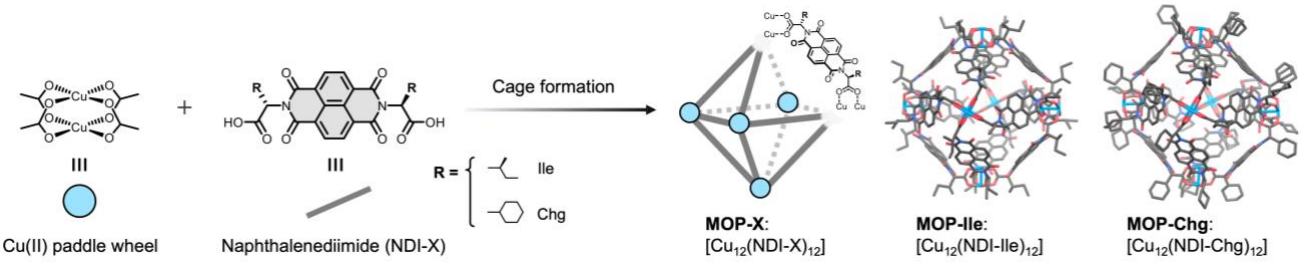

Figure 2. Schematic illustration of the synthesis of octahedral MOP, $[Cu_{12}(NDI\text{-}X)_{12}]$, from its building blocks. From left to right: a stick model with the chemical structure of the NDI linker (X = amino acid codes), **MOP-Ile**, and **MOP-Chg**.

Non-covalent intermolecular interactions have been known to be strongly influenced by solvent molecules.[28] To achieve the 1D self-assembly of MOPs through supramolecular polymerization, we screened the experimental conditions under different solvent environments. First, the as-synthesized crystal samples of **MOP-Ile** and **MOP-Chg** were washed with acetone and dried under vacuum at room temperature, which afforded amorphous powders of **MOP-Ile** (**Bulk-Ile**) and **MOP-Chg** (**Bulk-Chg**) (Figure S1). The resulting powders were fully dissolved in suitable solvents. **Bulk-Ile** readily dissolved in *N,N*-Dimethylformamide (DMF), while **Bulk-Chg** showed limited solubility in DMF and was therefore dissolved in *N,N*-Dimethylacetamide (DMA). These MOP solutions were mixed with 21 different counter solvents to investigate the precipitation behavior.

Both MOP systems showed two distinct precipitation behaviors depending on the counter solvent added. In the case of **MOP-Ile**, the addition of 1-butanol, cyclohexane, diethyl ether, dimethyl sulfoxide, 1,4-dioxane, hexane, 1-pentanol, tetrahydrofuran, or toluene resulted in the direct formation of crystals with octahedral morphology (**Crystal Oc-Ile**) within 24 hours (Figure 3a,b). In contrast, when methanol, acetonitrile, ethanol, nitromethane, or isopropanol was introduced, the mixture gradually became more viscous and ultimately formed a self-supporting gel (**Gel-Ile**)(Figure 3c). After two weeks at room temperature, **Gel-Ile** began to produce hexagonal pillar-shaped crystals (**Crystal Hp-Ile**), and it was fully transformed into the crystals within one month (Figure 3d). This gel-to-crystal transition strongly suggests that **Gel-Ile** corresponds to a metastable state, and it gradually transforms into the most stable crystalline state over time. Notably, increasing either the MOP concentration or the temperature accelerated the crystallization process.

MOP-Chg showed similar assembly behavior to that of **MOP-Ile.** The introduction of 1,4-dioxane and tetrahydrofuran drove direct crystallization to form plate-like crystals (**Crystal Pc-Chg**) within 24 hours (Figure S5a). On the other hand, the addition of methanol, acetonitrile, ethanol, nitromethane, nitroethane, acetone, isopropanol, or *tert*-butanol led to the formation of a self-supporting gel (**Gel-Chg**) (Figure S5b). This gel was subsequently transformed into rhombic crystals (**Crystal Rc-Chg**) within ten minutes (Figure S5c). Compared to **MOP-Ile**, **MOP-Chg** tend to remain soluble under a wider range of conditions,

To gain deeper insight into these solvent-dependent behaviors, we employed Hansen solubility parameters (HSPs).[29] HSPs decompose the total solubility parameter into three components: London dispersion forces (δ_D), dipole–dipole interactions (δ_P), and hydrogen bonding interactions (δ_H). These parameters provide a useful measure of the intermolecular interaction, allowing us to estimate the conditions that drive the desired self-assembly.[30,31] For mixed solvent systems, the HSPs can be approximated by the volume-weighted average of each solvent. We calculated the HSPs of the binary solvent systems used for MOP assembly (Table S3). Then, bivariate scatter plots were generated for each pair of δ_D, δ_P, and δ_H based on the HSPs (Figure S6).

By analyzing the solvent-dependent morphological differences using HSPs, the polarity and dispersive components of the solvents were found to play an important role in determining the resulting morphology. First, for data points of each solvent in the bivariate scatter plots obtained above, we labeled them according to the resulting morphology; solvent conditions that led to direct crystallization (e.g., **Crystal Oc-Ile** and **Crystal Pc-Chg**) were denoted by blue triangles, those that yielded gels prior to crystallization (e.g., **Crystal Hp-Ile** and **Crystal Rc-Chg**) were denoted by red circles, and those with no precipitation were indicated by black crosses (Figure S7). As a result, a clear trend was observed in the δ_D–δ_P plots: blue triangles were associated with solvents of relatively low polarity or strong dispersion, whereas red circles appeared under highly polar and weakly dispersive conditions (Figure 3e and S7). For instance, in the case of **MOP-Ile**, solvents of relatively low polarity or strong dispersion (δ_P < 12.1 $MPa^{1/2}$ or δ_D > 17.1 $MPa^{1/2}$) tended to assemble MOP molecules into **Crystal Oc-Ile**, whereas highly polar and weakly dispersive solvents (δ_P > 12.1 $MPa^{1/2}$ and δ_D < 17.1 $MPa^{1/2}$) led to gel formation followed by crystallization into **Crystal Hp-Ile**. A similar trend was also seen in **MOP-Chg** system.

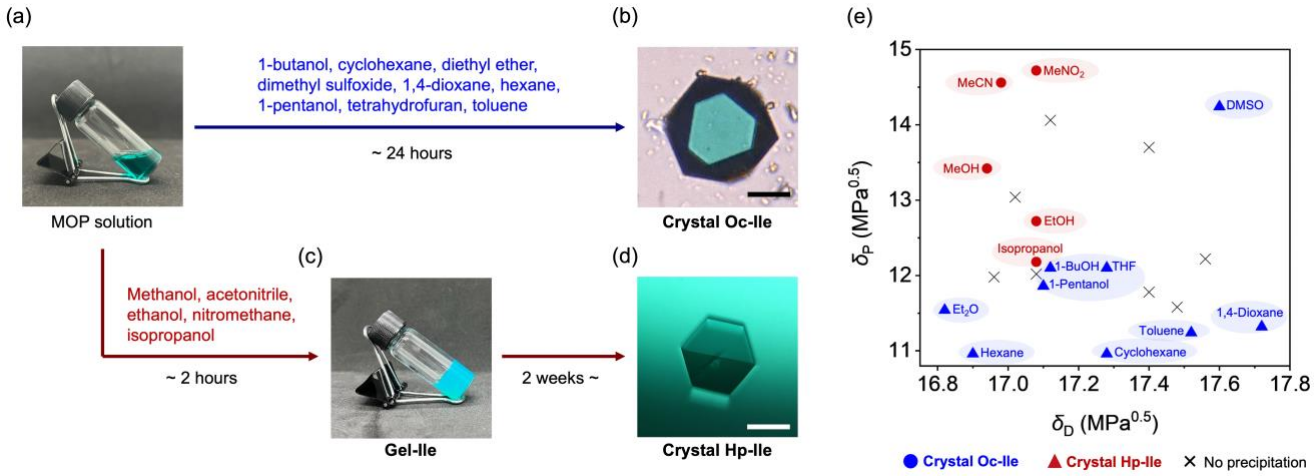

Figure 3. (a)When solvents such as 1-butanol, Cyclohexane, Diethyl ether, Dimethyl sulfoxide, 1,4-dioxane, Hexane, 1-pentanol, Tetrahydrofuran, or Toluene were added as a poor solvent, (b) the octahedral crystal (**Crystal Oc-Ile**) was directly obtained (scale bar: 200 μm). (c) After adding Acetonitrile, Ethanol, Nitromethane, 2-propanol, or Methanol, a self-supporting **Gel-Ile** was formed, (d) followed by hexagonal prismatic crystal (**Crystal Hp-Ile**) formation (scale bar: 200 μm). (e) Scatter plot (δ_D–δ_P) representing the morphology of **MOP-Ile** assemblies under 21 different solvent conditions. The 21 solvent conditions refer to mixtures of DMF and 21 different poor solvents (DMF/poor solvent = 4/1 v/v). The blue triangle (▲) indicates the formation of **Crystal Oc-Ile**, while the red circle (●) represents the formation of **Gel-Ile**, which subsequently undergoes a phase transition to **Crystal Hp-Ile**. × represents conditions where no precipitation was observed.

Subsequent SC-XRD analysis revealed that the octahedral structure of **MOP-Ile** and **MOP-Chg** was retained in all the crystals obtained after the supramolecular assembly. However, the resulting crystals exhibited entirely distinct molecular packings. In **Crystal Oc-Ile** formed under low-polar or strongly dispersive solvent, neighboring **MOP-Ile** molecules formed an edge-to-edge interaction between adjacent octahedra through their amino acid side chains. In this arrangement, the NDI planes faced each other, similar to those observed in **Pristine-Ile** and **Pristine-Chg** (Figure 4a). Furthermore, this interaction was accompanied by a relatively large intermolecular space between the NDI planes, where residual electron density was observed. This indicates the presence of solvent molecules occupying the intermolecular space between MOPs. An octahedron has twelve edges; as a result of twelve isotropically distributed edge-to-edge interactions around each **MOP-Ile**, they were crystallized in the space group *F*432 (Figure 4c,d).

On the other hand, in **Crystal Hp-Ile**, which was derived from **Gel-Ile** in polar and weakly dispersive solvents, the adjacent MOP molecules interacted through the NDI plane and amino acid side chains (Figure 4b). This corresponds to a face-to-face interaction through the triangular windows of the octahedron. In each MOP, two diagonally opposite faces out of eight participate in intermolecular interactions. Consequently, **MOP-Ile** assembled anisotropically, forming linear chains along the *c*-axis (Figure 4e,f). A closer inspection of the copper atoms at the vertices revealed that **MOP-Ile** underwent a 120° rotation over six MOP units within a chain. These chains were further assembled and adopted the space group *P*3. Due to its exceptionally large unit cell volume of 220 nm^3 and low symmetry, the detailed structural determination of the isoleucine side chains was not possible.

Similar trend was also observed for **MOP-Chg**. Within **Crystal Pc-Chg**, which was obtained under low-polar or strongly dispersive solvent conditions, the adjacent **MOP-Chg** exhibited edge-to-edge interactions, with comparably large intermolecular space (Figure SX). Such edge-to-edge interactions led to the assembly of MOP molecules in the space group $P2_1$, resulting in a distorted face-centered cubic (FCC) lattice. On the other hand, **Crystal Rc-Chg**, formed via **Gel-Chg** under highly polar and weakly dispersive conditions, showed anisotropic molecular assemblies similar to those of **Crystal Hp-Ile** (Figure SX). Unlike the continuous 1D chains observed for **MOP-Ile**, **MOP-Chg** assembled into shorter chains composed of three MOP molecules. Within this trimeric chain structure, MOP-Chg underwent a 66° rotation over three MOP units within a chain.

To understand the nature of interactions between MOPs, we performed energy decomposition analysis (EDA) based on DFT calculations (Figure SX).[24,32,33] This analysis was conducted based on the crystal structures of **Crystal Oc-Ile** and **Crystal Rc-Chg**, in which the atomic positions of the amino acid side chains were clearly determined. The fragment used was prepared by extracting a pair of NDI linkers from adjacent MOPs in the crystal structures. The

results showed that the stabilization energy between two NDI linkers in **Crystal Oc-Ile** was 36 kJ mol^{-1}, while that for **Crystal Rc-Chg** was 88 kJ mol^{-1}. Despite differences in interaction strength, dispersion forces contributed approximately 90% of the total stabilization energy in both systems, confirming that van der Waals forces are the dominant interaction.

Based on the above results, it was found to be crucial to employ solvents with a low dispersive component and high polarity for the 1D assembly of MOPs. In other words, the selective synthesis of 1D assemblies can be achieved by suppressing dispersive interactions between the solvent and MOP molecules, while enhancing polarity to promote intermolecular interactions between MOPs. This interpretation is consistent with structural observations and EDA calculations: in crystals forming 1D chains (**Crystal Hp-Ile** and **Crystal Rc-Chg**), neighboring MOP molecules interact more closely and strongly, whereas in other crystals (**Crystal Oc-Ile** and **Crystal Pc-Chg**), solvent molecules penetrate between the MOPs, resulting in weaker intermolecular interactions.

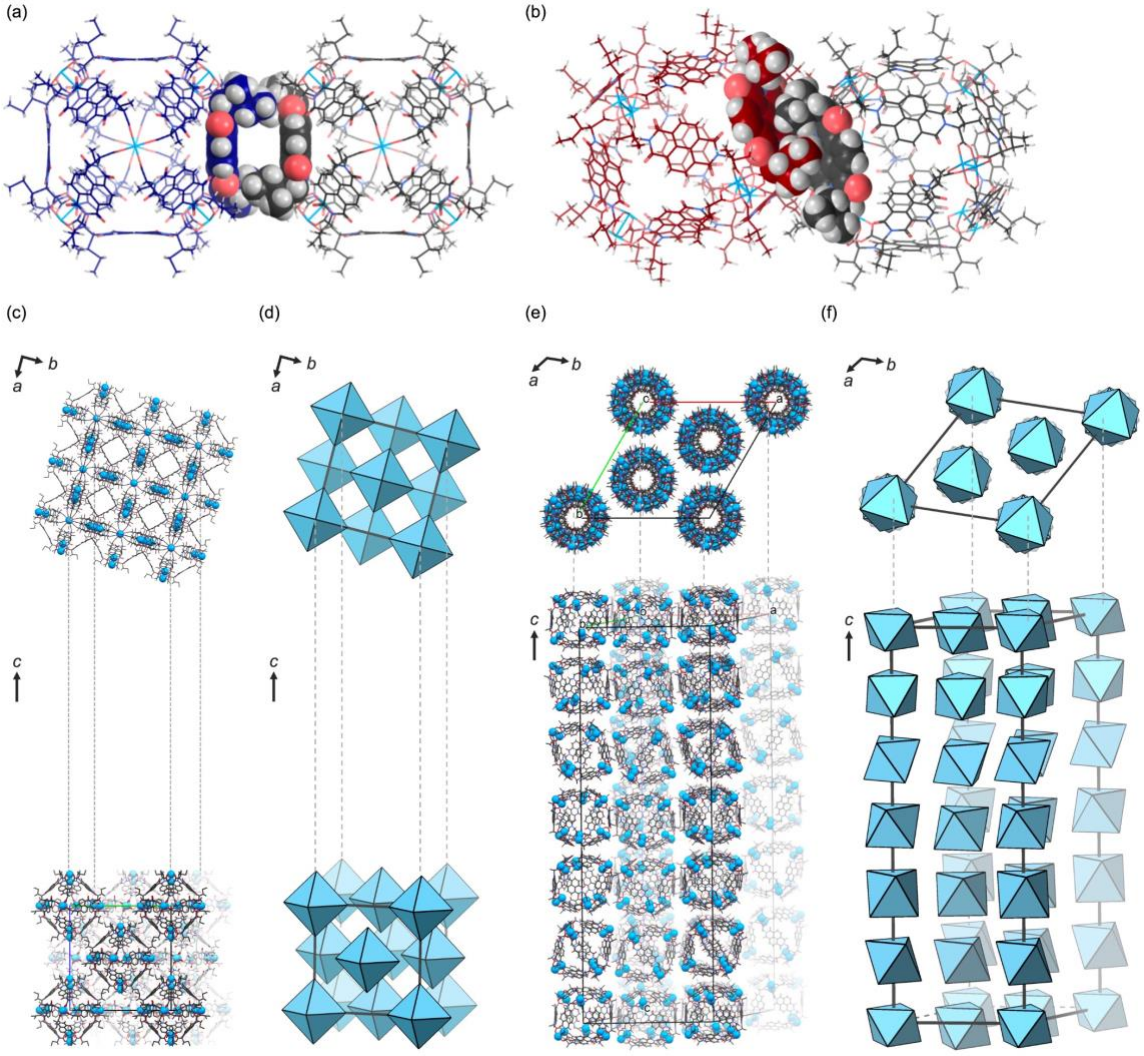

Figure 4. Visualization of intermolecular interactions and molecular packing in each crystal based on single-crystal X-ray structural analysis. (a) The interaction between the neighboring **MOP-Ile** within the crystal of **Crystal Oc-Ile** (from DMF/1,4-dioxane). The regions expected to participate in intermolecular interactions are highlighted using a space-filling model. (b) The interaction between the neighboring **MOP-Ile** within the crystal of **Crystal Hp-Ile** (from DMF/Methanol). (c,d) Molecular packing of **MOP-Ile** within the unit cell of **Crystal Oc-Ile**. The molecular structures are represented in a wire model with the copper atoms highlighted for better visibility. A blue octahedron is drawn based on the atomic coordinates of six Cu atoms in a MOP molecule to facilitate visualization of the molecular arrangement in a unit cell. (e,f) Molecular packing of **MOP-Ile** within the unit cell of **Crystal Hp-Ile**. The MOP chains were aligned parallel to the *c*-axis.

Reversible nature of MOP-based supramolecular gels. Gels can be classified as chemical or physical, depending on the nature of the cross-linking. Chemical gels are covalently bonded and typically rigid,[34] whereas physical gels are held

together by non-covalent interactions, allowing reversible structural changes in response to external stimuli.[35–37] Since the gels obtained in the previous section were formed solely through non-covalent interactions, we measured their responses to external stimuli, expecting them to behave as physical gels. The gels used in the following tests (**Gel-Ile** and **Gel-Chg**) were synthesized using methanol as the poor solvent. Specifically, 3.5 mM solutions of **MOP-Ile** and **MOP-Chg** were mixed with methanol at a volume ratio of 4:1 (MOP solution/methanol, v/v) and mixed thoroughly. Upon addition, the solutions gradually became more viscous, eventually forming **Gel-Ile** and **Gel-Chg** (Figure SX). In the case of **Gel-Ile**, gelation occurred approximately 2 hours after mixing, whereas **Gel-Chg** gelated within about 1 minute. These gels exhibited a reversible sol–gel transition in response to external stimuli. When these gels were subjected to mechanical stress using a vortex mixer, they immediately transformed into a fluid sol state (Figure SX). Subsequently, when left undisturbed at room temperature, the sols gradually increased in viscosity and finally returned to a gel state.

To quantitatively evaluate the above-mentioned reversible nature, shearing rheological measurements were conducted on **Gel-Ile**. Due to the rapid gel-to-crystal transition in **Gel-Chg**, the measurements were conducted only on **Gel-Ile** to ensure sample homogeneity during the measurements. **Gel-Ile** was prepared *in situ* on the rheometer to prevent any alteration in the internal structure. A mixture of the **MOP-Ile** solution and methanol was placed onto the rheometer and left to stand for 2 hours. We first conducted the angular frequency sweep test, in which the angular frequency was varied from ω = 1 to 500 rad s^{-1} at a fixed strain amplitude of γ = 0.01%, to quantify the storage (G') and loss (G'') moduli (Figure 5a). As a result, the sample exhibited frequency-independent G', which was an order of magnitude higher than G'', confirming that the sample was in a gel state. In rheological analysis, the ratio of G'' to G' is often expressed as $\tan\delta$ (= G''/G'), which indicates the relative contribution of viscous and elastic components.[38] When $\tan\delta$ < 1, the material behaves predominantly elastically (solid-like), whereas $\tan\delta$ > 1 indicates viscous dominance (liquid-like). Accordingly, the viscoelastic properties discussed below are described in terms of $\tan\delta$.

To investigate the mechanical response under applied stress, strain amplitude sweep measurements were performed by fixing the oscillatory frequency at ω = 10 rad s^{-1} and gradually increasing the strain amplitude from γ = 0.001% to 30% (Figure 5b). As a result, within the strain range of 0.005% < γ < 0.1%, G' remained constant regardless of strain amplitude, indicating a linear viscoelastic response with $\tan\delta$ < 1. When the strain exceeded γ = 0.3%, G' began to deviate from linearity, and at strains beyond γ = 3.5%, $\tan\delta$ surpassed 1, indicating a transition from solid-like to liquid-like behavior. These results suggest a gel-to-sol transition occurs at strain levels exceeding γ = 3.5%.

Based on the results of the strain amplitude sweep test, an interval measurement was performed on **Gel-Ile** by alternately applying strains of γ = 0.01% and 10% (Figure 4c). Initially, a small strain of γ = 0.01% was applied for 5 minutes, followed by a larger strain of γ = 10% for another 5 minutes. Subsequently, the recovery process was monitored for 20 minutes. Under the small strain of γ = 0.01%, the condition G' > G'', that is, $\tan\delta$ < 1, was maintained, indicating that the sample remained in the gel state. After applying a larger strain of γ = 10%, the condition reversed to G' < G'', corresponding to $\tan\delta$ > 1, reflecting a transition to the sol state. When the strain was subsequently reduced to γ = 0.01% and held for 20 minutes, the sample recovered to a solid-like state, as indicated by $\tan\delta$ < 1. These results demonstrate that **Gel-Ile** has a thixotropic nature, undergoing a reversible sol–gel transition in response to mechanical stress. This reversibility is likely attributed to the non-covalent interactions between MOPs.

As an application of this reversible nature, we carried out a mold shaping experiment. For this experiment, we used **Gel-Ile** prepared at 7.0 mM **MOP-Ile** concentration, as it exhibited a higher G' value than the 3.5 mM sample (Figure SX). Specifically, the G' value increased from approximately 2 kPa at 3.5 mM to 10 kPa at 7.0 mM. The as-synthesized **Gel-Ile** was first converted into a sol state by applying mechanical stress and then poured into a flower-shaped mold (Figure 4d). After approximately 15 minutes, it gelated, resulting in a flower-shaped gel. Mechanical stress was subsequently applied to this gel, and the resulting sol was transferred into a star-shaped mold, yielding a star-shaped gel. This demonstration highlights the processing versatility of **Gel-Ile**.

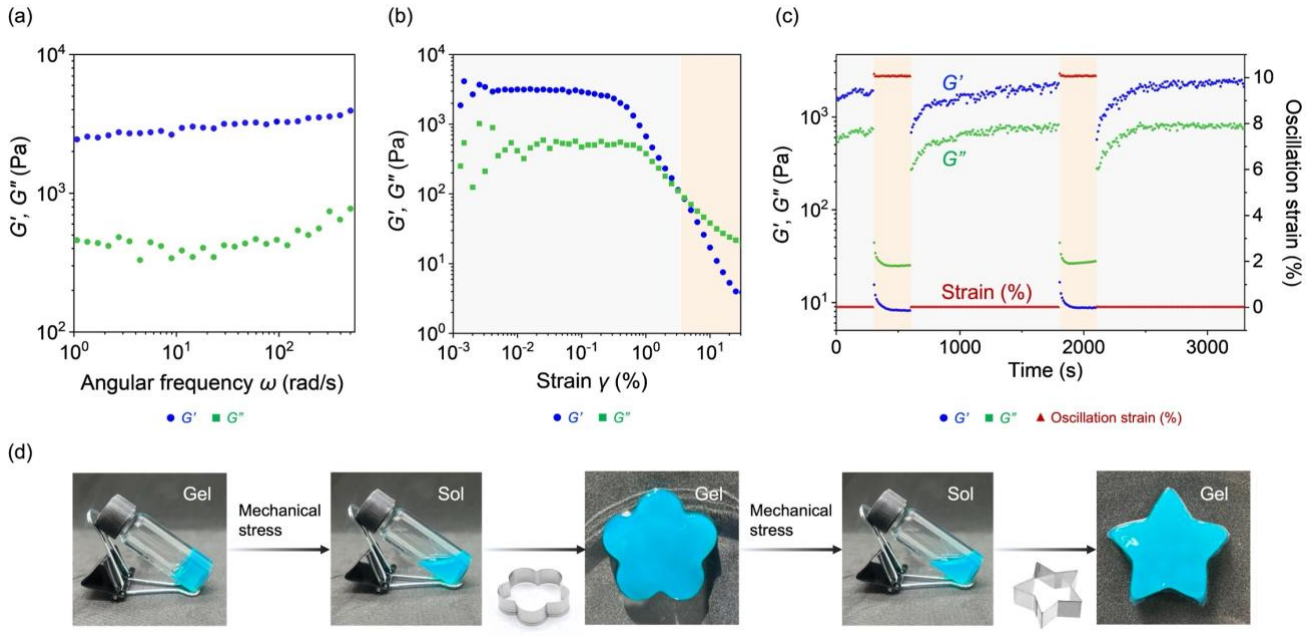

Figure 5. Results of the shearing rheological measurements for **Gel-Ile**. In both figures, the storage modulus G' is represented by blue circles, while the loss modulus G'' is represented by green square markers. (a) Frequency sweep measurement conducted at $\gamma = 0.01\%$. The scanned frequency range was from $\omega = 1$ to 500 rad/s. (b) Strain sweep measurement conducted at $\omega = 10$ rad/s. The scanned strain range was 0.001 to 30%. At around $\gamma = 3.5\%$, G' became smaller than G'', indicating a gel-to-sol transition. (c) Step strain experiment conducted at $\omega = 10$ rad/s. The applied strain value is represented as red triangles. Based on the strain sweep measurement results, a strain of 0.01% was applied for the first 5 minutes, followed by a 10% strain for 5 minutes. Recovery of the sample was then monitored over 20 minutes. After that, a 10% strain was applied again for 5 minutes, followed by another 20-minute period to observe the reversible recovery behavior. (d) Mold shaping experiments of **Gel-Ile**. The as-synthesized **Gel-Ile** (7.0 mM) was applied mechanical stress using a vortex mixer for 10 seconds to obtain a fluidic sol. This sol was then transferred into a flower-shaped mold. After being left at room temperature for a while, a flower-shaped gel was obtained. Further mechanical stress was applied to the flower-shaped gel to convert it into a sol, which was poured into a star-shaped mold. As a result, a star-shaped gel was obtained, demonstrating the high moldability of **Gel-Ile**.

Microscopic structure of MOP-based supramolecular polymers. To investigate the internal structure of the obtained gels, we conducted microscopic observations. Following the method described in the preceding section, methanol was added to a 3.5 mM MOP solution at a volume ratio of 4:1 (MOP solution/methanol, v/v) to synthesize **Gel-Ile** and **Gel-Chg**, respectively (Figure 5). The resulting gels were transferred into vials containing 10 mL of fresh isopropanol, and the original solvent was gradually replaced with isopropanol over a period of three days. While the gels without solvent exchange crystallized within several weeks, those subjected to solvent exchange remained amorphous for more than six months. Then, isopropanol was completely removed by supercritical CO_2 drying, yielding the corresponding aerogels, **Aerogel-Ile** for **MOP-Ile** and **Aerogel-Chg** for **MOP-Chg** (Figure 5, SX). Scanning electron microscopy (SEM) analysis of these aerogels revealed anisotropic fibrous structures entangled together (Figure 5). This morphology is entirely different from that of previously reported MOP-based gel materials.[19,39–43] In addition, meso- to macroscopic spaces were observed between the fibers. The width of the one-dimensional fibrous structures was defined as the dimension perpendicular to their longitudinal axis. Measurement of 200 points in fiber widths showed that the average width of the **Aerogel-Ile** fibers was 14.8 ± 2.2 nm, and that of the **Aerogel-Chg** fibers was 9.95 ± 1.4 nm (Figure SX). Considering that the molecular diameter of a single MOP is approximately 2.7 nm, the average fiber width corresponds to a length equivalent to about three to six MOP molecules. Moreover, the deviation d remained within the size of a single MOP unit, indicating a high degree of uniformity.

To further investigate the internal structure of fibers, cryogenic electron microscopy (Cryo-EM) observation was conducted. Cryo-EM is an essential technique for probing soft materials that are highly sensitive to solvent removal and electron beam damage. In accordance with the previous study,[44] a suspension of **Gel-Ile** in MeCN (0.17 mM) was applied to glow-discharged holey carbon film-coated copper grids (Quantifoil R2/1) and plunge-frozen using a Vitrobot Mark IV (FEI) for Cryo-EM observation. After several trials, optimized vitrification conditions were established and are summarized in Table SX. Here, only the **Gel-Ile** was used for measurements due to concerns about the potential crystallization and instability of **Gel-Chg**. As a result, fibrous structures similar to those observed in the SEM analysis were also observed (Figure 5). From this

image, the thickness of 200 fibers was measured, and the average value was consistent with that obtained from SEM analysis (Figure SX). Despite using a highly diluted sample, it was challenging to visualize well-separated individual fibers. At concentrations lower than 0.17 mM, the number of fibers was insufficient for mutual stabilization, resulting in vibration during imaging and a further decrease in image quality. Although the majority of the fibers were overlapping, some regions with non-overlapping fibers were also identified (Figure 5). Upon closer examination of this region, contrast differences were observed, with darker areas interspersed with relatively lighter regions. The distances between adjacent dark spots were measured at several points and averaged to be 2.5 ± 0.24 nm, which is in good agreement with the molecular diameter of the **MOP-Ile** (Figure SX). These darker spots are therefore presumed to correspond to the vertices composed of copper paddlewheel units, where the electron density is relatively high. In contrast, the lighter regions likely represent organic linkers with lower electron density, as discussed in a previous report.[44]

Subsequent powder X-ray diffraction (PXRD) measurements revealed that these aerogels were amorphous in nature (Figure SX). A broad shoulder was observed in the low-angle region ($2\theta < 3°$). Therefore, we conducted a further investigation by small-angle X-ray scattering (SAXS). Based on SEM observations, the raw SAXS data were fitted using a long cylinder model. As a result, the radii of the structural features were estimated to be 9.60 ± 0.0231 nm for **Aerogel-Ile** and 7.31 ± 0.0174 nm for **Aerogel-Chg** (Figure SX). These correspond to diameters of approximately 19.2 nm and 14.6 nm, respectively, which are in good agreement with the values observed by SEM and Cryo-EM.

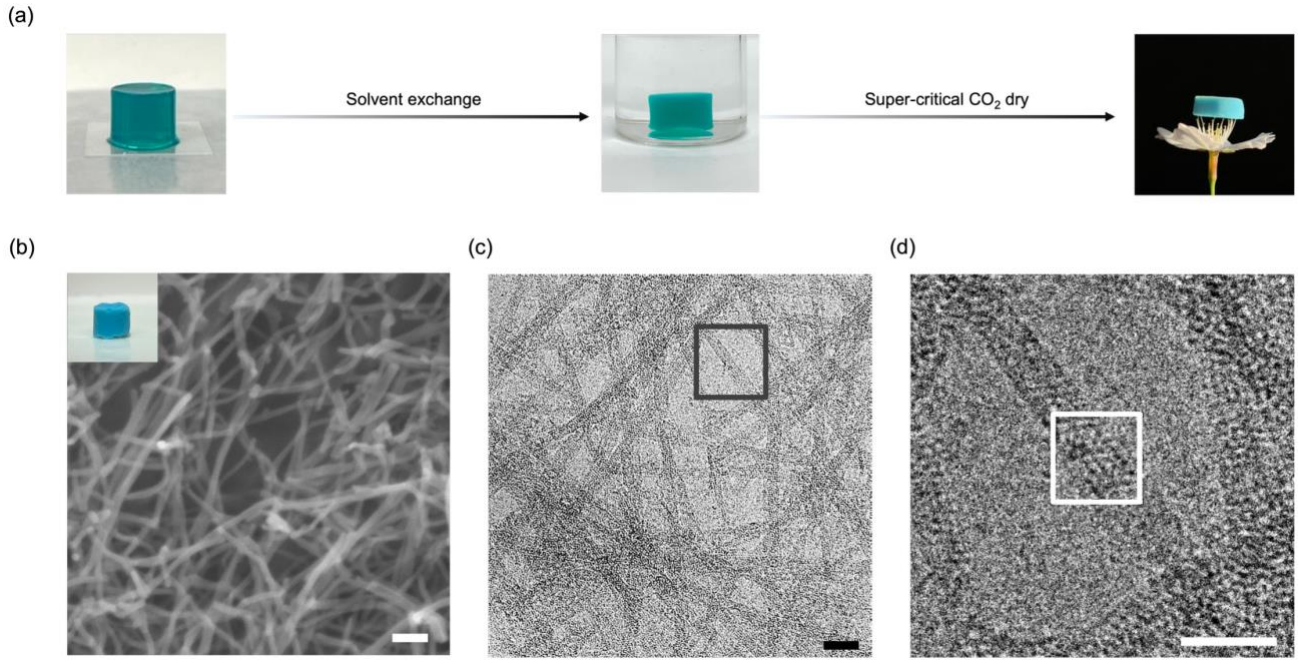

Figure 6. (a) Procedure for subjecting as-synthesized gels to supercritical CO_2 drying. From left to right: as-synthesized **Gel-Ile**, gel immersed in isopropanol for solvent exchange, and **Aerogel-Ile** after supercritical CO_2 drying. (b) The SEM observation of **Aerogel-Ile** (inset: **Aerogel-Ile**, scale bar 100 nm). Anisotropic fibrous structure was observed intertwining and forming a network. The width measurements of 200 points resulted in an average value of 14.8 $\pm$ 2.2 nm. (c) The Cryo-EM observation of **Aerogel-Ile** (scale bar: 50 nm) Throughout the entire image, fibrous structures similar to those observed in SEM were found, along with unique dot-like patterns. The width measurements of 200 points resulted in an average value of 14.7 ± 2.3 nm. (d) A magnified view (scale bar: 25 nm). The area enclosed by the white frame shows a single fiber.

Sorption and mechanical properties of MOP-based supramolecular polymers. Carbon dioxide and nitrogen sorption measurements were conducted to investigate the porosity of the MOP-based supramolecular polymers. Here, we prepared **Aerogel-Ile**, **Aerogel-Chg**, **Crystal Hp-Ile**, and **Crystal Rc-Chg** for comparison. The carbon dioxide isotherms of **Aerogel-Ile**, **Aerogel-Chg**, **Crystal Hp-Ile**, and **Crystal Rc-Chg** showed a type I profile, with saturation of the gas uptake of 69.1 $cm^3 g^{-1}$, 73.6 $cm^3 g^{-1}$, 73.6 $cm^3 g^{-1}$, and 86.4 $cm^3 g^{-1}$ at P/P_0 = 0.1, respectively (Figure 6). This comparison of the adsorption amounts at P/P_0 = 0.1 clearly indicates that these four samples displayed comparable adsorption behavior. The subsequent nitrogen sorption isotherms of **Aerogel-Ile** and **Aerogel-Chg** exhibited type II profiles, with gas uptake saturating at 195 $cm^3 g^{-1}$ and 155 $cm^3 g^{-1}$, respectively, at P/P_0 = 0.1 (Figure 6). In contrast,

Crystal Hp-Ile showed a type I isotherm with a saturation uptake of 140 $cm^3\,g^{-1}$ at the same relative pressure, while **Crystal Rc-Chg** exhibited negligible adsorption. The Brunauer–Emmett–Teller (BET) surface areas were determined to be 786 $m^2\,g^{-1}$ for **Aerogel-Ile**, 627 $m^2\,g^{-1}$ for **Aerogel-Chg**, and 555 $m^2\,g^{-1}$ for **Crystal-Hp-Ile** by using the BETSI program (Figure SX).[45]

The aerogels and crystals obtained from corresponding gels in this study share identical chemical compositions; the only difference lies in the arrangement of MOP molecules. Specifically, the aerogels do not contain any crosslinkers or additives, and therefore, the gas uptake per unit mass is expected to be comparable. This expectation is well supported by the carbon dioxide sorption isotherms. Due to its smaller kinetic diameter relative to nitrogen, carbon dioxide adsorption is considered to be predominantly governed by the intrinsic microporosity of MOPs, resulting in similar isotherm profiles among all samples. In contrast, the nitrogen adsorption measurements reflect the presence of meso- and macropores in the aerogels, which account for the higher uptake relative to their crystalline samples. While both **Crystal Hp-Ile** and **Crystal Rc-Chg** retained partial crystallinity before and after gas adsorption, only the latter exhibited negligible nitrogen uptake (Figure SX), suggesting that differences in molecular packing play a key role. Single-crystal structural analysis revealed that **MOP-Ile** in **Crystal Hp-Ile** forms continuous one-dimensional channels, whereas **MOP-Chg** in **Crystal Rc-Chg** assembles into trimer-like units, introducing periodic structural discontinuities. This disrupted channel connectivity might hinder nitrogen diffusion, accounting for the suppressed adsorption observed in **Crystal Rc-Chg**.

The mechanical flexibility of the aerogel samples was evaluated through uniaxial compression measurements. Figure 6 shows stress–strain curves obtained from **Aerogel-Ile** and **Aerogel-Chg**. In the case of **Aerogel-Ile**, the stress (σ) increased linearly with compressive strain (ε) up to the yield point, indicated by a star symbol. Within this elastic regime, the Young's moduli (E) were determined to be E = 41.0 kPa. Beyond the elastic regime, materials typically undergo plastic deformation, characterized by irreversible shape changes even after unloading. Further compression typically results in the appearance of discontinuities in the stress–strain curve, accompanied by the formation of cracks or fractures. The strain at which such a fracture occurs is defined as a fracture strain (ε_f). This parameter serves as a critical indicator of a material's capacity to undergo deformation prior to the fracture point. Further compression on **Aerogel-Ile** beyond the yield point led to plastic deformation; however, unlike many conventional porous materials, no fracture point was observed even at a strain of ε = 87.0%, at which point the measurement was terminated (Figure 6). By integrating the stress–strain curve, the toughness (T) of **Aerogel-Ile** was calculated to be 19.6 $kJ\,m^{-3}$. For **Aerogel-Chg**, the Young's moduli were determined to be E = 21.2 kPa. However, the fracture occurred at a strain of ε = 17.9% (Figure 6), and the corresponding toughness was determined to be 0.22 $kJ\,m^{-3}$.

Although the difference between **Aerogel-Ile** and **Aerogel-Chg** in the macroscopic mechanical behavior is difficult to determine, they are presumably attributed to subtle variations in fiber thickness and curvature, as well as the internal arrangement of MOPs within the fibers. Nevertheless, both aerogels exhibited greater flexibility than conventional porous materials. These materials combine the uniform porosity typical of crystalline porous materials with a level of toughness comparable to that of rubbers, metals, alloys, and polymers.[46] As a result, we successfully synthesized a new class of porous materials with both permanent microporosity and remarkable flexibility. This demonstrates that by controlling the molecular packing, mechanical flexibility can be imparted even to materials that have traditionally been regarded as brittle.

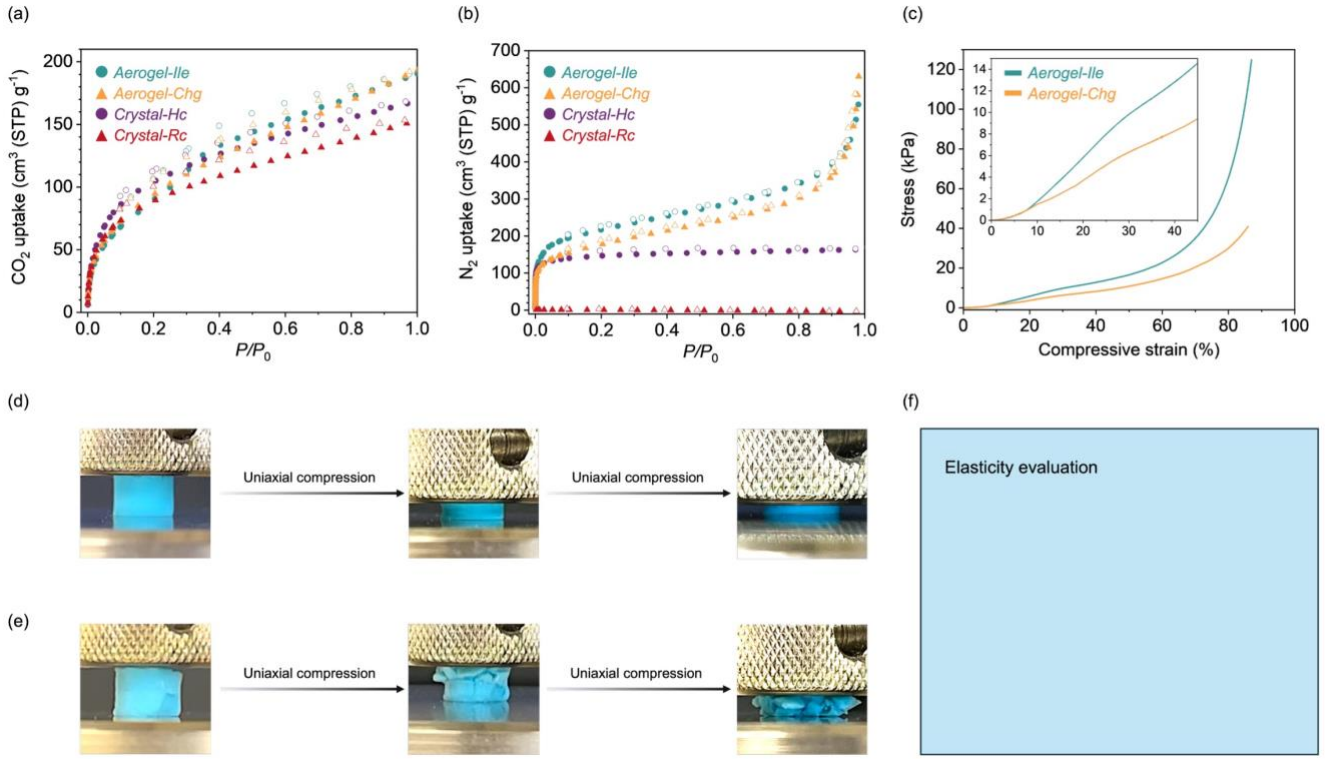

Figure 7. (a) Carbon dioxide adsorption isotherm at 195 K and (b) nitrogen adsorption isotherm at 77 K for **Aerogel-Ile**, **Aerogel-Chg**, **Crystal Hp-Ile**, and **Crystal Rc-Chg**. (c) Uniaxial compression measurements for **Aerogel-Ile** and **Aerogel-Chg**. (inset: an enlarged view of the strain value $\varepsilon = 0$ to 45%). The initial nonlinearity of the stress-strain curve (at strain values below 10%) is attributed to the unevenness of the aerogel surface. (d) **Aerogel-Ile** before compression (left), during compression (middle), and after 85% compression (right). (e) **Aerogel-Chg** before compression (left), during compression (middle), and after 85% compression (right). (f) Stress–strain curve obtained from a uniaxial compression test with subsequent unloading to examine the elastic recovery.

CONCLUSION

In conclusion, we successfully synthesized porous supramolecular polymers with remarkable mechanical flexibility via one-dimensional self-assembly of MOPs. Quantitative analysis combining HSPs and SC-XRD measurements clarified that the formation of one-dimensional assembly requires the addition of poor solvents with high polarity and low dispersive forces. Subsequent energy decomposition analysis suggested that these solvents facilitate stronger intermolecular interactions between MOPs. This suggests that even van der Waals interactions, which are generally considered non-directional, can be harnessed to control molecular assembly by appropriately selecting solvent conditions. Compared to the brittle fracture behavior typically observed in functional materials with rigid three-dimensional structures, the pronounced mechanical flexibility achieved here is strongly attributed to the anisotropic, one-dimensional assembly supported by non-covalent interactions. This approach, which introduces mechanical flexibility by puzzling hollow supramolecular building blocks, offers a new design strategy for creating porous materials with enhanced mechanical flexibility.

ASSOCIATED CONTENT

Supporting Information

The Supporting Information is available free of charge on the ACS Publications website.

Full details of sample preparation, characterization, and simulation results (PDF)

AUTHOR INFORMATION

Corresponding Author

* shuhei.furukawa@icems.kyoto-u.ac.jp

Present Addresses

[a] Present address: (Shun)
[b] Present address: (Kuzumoto, Aoyama)
[c] Present address: (Glen)

Notes

The authors declare no competing financial interest.

ACKNOWLEDGMENT

Synchrotron X-ray diffraction experiments on A, B and C were performed on the BL40XU beamline at the SPring-8 facility

(2023B1307) and D on the BL02B1 (2023B1617) for SC-XRD. PXRD measurements were conducted at the BL02B2. We thank the beamline scientists for their helpful discussions. A. M. acknowledges …. The authors thank the iCeMS Analysis Center for access to analytical instruments.

REFERENCES

(1) Drory, M. D.; Gardinier, C. F.; Speck, J. S. Fracture Toughness of Chemically Vapor-Deposited Diamond. *J. Am. Ceram. Soc.* **1991**, *74* (12), 3148–3150.

(2) Telling, R. H.; Pickard, C. J.; Payne, M. C.; Field, J. E. Theoretical Strength and Cleavage of Diamond. *Phys. Rev. Lett.* **2000**, *84* (22), 5160–5163.

(3) Hess, P. The Mechanical Properties of Various Chemical Vapor Deposition Diamond Structures Compared to the Ideal Single Crystal. *J. Appl. Phys.* **2012**, *111* (5), 051101.

(4) Lee, C.; Wei, X.; Kysar, J.; Hone, J. Measurement of the Elastic Properties and Intrinsic Strength of Monolayer Graphene. *Science* **2008**, *321*, 385–388.

(5) Han, E.; Yu, J.; Annevelink, E.; Son, J.; Kang, D. A.; Watanabe, K.; Taniguchi, T.; Ertekin, E.; Huang, P. Y.; van der Zande, A. M. Ultrasoft Slip-Mediated Bending in Few-Layer Graphene. *Nat. Mater.* **2020**, *19* (3), 305–309.

(6) Iijima, S.; Brabec, C.; Maiti, A.; Bernholc, J. Structural Flexibility of Carbon Nanotubes. *J. Chem. Phys.* **1996**, *104* (5), 2089–2092.

(7) Yu, M.-F.; Lourie, O.; Dyer, M. J.; Moloni, K.; Kelly, T.; Ruoff, R. Strength and Breaking Mechanism of Multiwalled Carbon Nanotubes under Tensile Load. *Science* **2000**, *287* (5453), 637–640.

(8) Phillips, J. C. Topology of Covalent Non-Crystalline Solids I: Short-Range Order in Chalcogenide Alloys. *J. Non Cryst. Solids* **1979**, *34* (2), 153–181.

(9) Awad, W. M.; Davies, D. W.; Kitagawa, D.; Mahmoud Halabi, J.; Al-Handawi, M. B.; Tahir, I.; Tong, F.; Campillo-Alvarado, G.; Shtukenberg, A. G.; Alkhidir, T.; Hagiwara, Y.; Almehairbi, M.; Lan, L.; Hasebe, S.; Karothu, D. P.; Mohamed, S.; Koshima, H.; Kobatake, S.; Diao, Y.; Chandrasekar, R.; Zhang, H.; Sun, C. C.; Bardeen, C.; Al-Kaysi, R. O.; Kahr, B.; Naumov, P. Mechanical Properties and Peculiarities of Molecular Crystals. *Chem. Soc. Rev.* **2023**, *52* (9), 3098–3169.

(10) Reddy, C. M.; Padmanabhan, K. A.; Desiraju, G. R. Structure−Property Correlations in Bending and Brittle Organic Crystals. *Cryst. Growth Des.* **2006**, *6* (12), 2720–2731.

(11) Aida, T.; Meijer, E. W.; Stupp, S. I. Functional Supramolecular Polymers. *Science* **2012**, *335* (6070), 813–817.

(12) Suzuki, R.; Karasawa, A.; Gomita, A.; Abe, M.; Kojima, K.; Tachibana, M. Unique Mechanical Properties of Gel-Incorporating Protein Crystals. *ACS Appl. Bio Mater.* **2023**, *6* (3), 965–972.

(13) Malay, A. D.; Suzuki, T.; Katashima, T.; Kono, N.; Arakawa, K.; Numata, K. Spider Silk Self-Assembly via Modular Liquid-Liquid Phase Separation and Nanofibrillation. *Sci. Adv.* **2020**, *6* (45), eabb6030.

(14) Fujita, D.; Ueda, Y.; Sato, S.; Yokoyama, H.; Mizuno, N.; Kumasaka, T.; Fujita, M. Self-Assembly of M 30 L 60 Icosidodecahedron. *Chem* **2016**, *1* (1), 91–101.

(15) Kolesnichenko, I. V.; Anslyn, E. V. Practical Applications of Supramolecular Chemistry. *Chem. Soc. Rev.* **2017**, *46* (9), 2385–2390.

(16) Eddaoudi, M.; Kim, J.; Wachter, J. B.; Chae, H. K.; O'Keeffe, M.; Yaghi, O. M. Porous Metal−Organic Polyhedra: 25 Å Cuboctahedron Constructed from 12 $Cu_2(CO_2)_4$ Paddle-Wheel Building Blocks. *J. Am. Chem. Soc.* **2001**, *123* (18), 4368–4369.

(17) Sudik, A. C.; Millward, A. R.; Ockwig, N. W.; Côté, A. P.; Kim, J.; Yaghi, O. M. Design, Synthesis, Structure, and Gas (N2, Ar, CO2, CH4, and H2) Sorption Properties of Porous Metal-Organic Tetrahedral and Heterocuboidal Polyhedra. *J. Am. Chem. Soc.* **2005**, *127* (19), 7110–7118.

(18) Tateishi, T.; Yoshimura, M.; Tokuda, S.; Matsuda, F.; Fujita, D.; Furukawa, S. Coordination/Metal–Organic Cages inside Out. *Coord. Chem. Rev.* **2022**, *467* (214612), 214612.

(19) Carné-Sánchez, A.; Craig, G. A.; Larpent, P.; Hirose, T.; Higuchi, M.; Kitagawa, S.; Matsuda, K.; Urayama, K.; Furukawa, S. Self-Assembly of Metal-Organic Polyhedra into Supramolecular Polymers with Intrinsic Microporosity. *Nat. Commun.* **2018**, *9* (1), 2506.

(20) Lee, B.; Park, I.-H.; Park, J. Bridging and Fixing Metal–Organic Cages. *ACS Mater. Lett.* **2022**, *4* (11), 2388–2393.

(21) Sánchez-González, E.; Tsang, M. Y.; Troyano, J.; Craig, G. A.; Furukawa, S. Assembling Metal-Organic Cages as Porous Materials. *Chem. Soc. Rev.* **2022**, *51* (12), 4876–4889.

(22) Khobotov-Bakishev, A.; Samanta, P.; Roztocki, K.; Albalad, J.; Royuela, S.; Furukawa, S.; Zamora, F.; Carné-Sánchez, A.; Maspoch, D. Post‐synthetic Modification of Aerogels Made of Covalent Cross‐linked Metal‐organic Polyhedra. *Adv. Funct. Mater.* **2023**. https://doi.org/10.1002/adfm.202312166.

(23) Lee, B.; Go, B.; Jung, B.; Park, J. Unlocking High Porosity: Post-Synthetic Solvothermal Treatment of Cu-Paddlewheel Based Metal-Organic Cages. *Small* **2024**, *20* (23), e2308393.

(24) Tokuda, S.; Furukawa, S. Three-Dimensional van Der Waals Open Frameworks. *Nat. Chem.* **2025**, *17* (5), 672–678.

(25) Mollick, S.; Mukherjee, S.; Kim, D.; Qiao, Z.; Desai, A. V.; Saha, R.; More, Y. D.; Jiang, J.; Lah, M. S.; Ghosh, S. K. Hydrophobic Shielding of Outer Surface: Enhancing the Chemical Stability of Metal-Organic Polyhedra. *Angew. Chem. Int. Ed.* **2019**, *58* (4), 1041–1045.

(26) Boer, S. A.; White, K. F.; Slater, B.; Emerson, A. J.; Knowles, G. P.; Donald, W. A.; Thornton, A. W.; Ladewig, B. P.; Bell, T. D. M.; Hill, M. R.; Chaffee, A. L.; Abrahams, B. F.; Turner, D. R. A Multifunctional, Charge-Neutral, Chiral Octahedral M12 L12 Cage. *Chem. Eur. J.* **2019**, *25* (36), 8489–8493.

(27) Kobaisi, M. A.; Bhosale, S. V.; Latham, K.; Raynor, A. M.; Bhosale, S. V. Functional Naphthalene Diimides: Synthesis, Properties, and Applications. *Chem. Rev.* **2016**, *116* (19), 11685–11796.

(28) Mabesoone, M. F. J.; Palmans, A. R. A.; Meijer, E. W. Solute-Solvent Interactions in Modern Physical Organic Chemistry: Supramolecular Polymers as a Muse. *J. Am. Chem. Soc.* **2020**, *142* (47), 19781–19798.

(29) Hansen, C. M. *Hansen Solubility Parameters: A User's Handbook, Second Edition*, 2nd ed.; CRC Press: Boca Raton, FL, 2007.

(30) Raynal, M.; Bouteiller, L. Organogel Formation Rationalized by Hansen Solubility Parameters. *Chem. Commun. (Camb.)* **2011**, *47* (29), 8271–8273.

(31) van der Tol, J. J. B.; Vantomme, G.; Meijer, E. W. Solvent-Induced Pathway Complexity of Supramolecular Polymerization Unveiled Using the Hansen Solubility Parameters. *J. Am. Chem. Soc.* **2023**, *145* (32), 17987–17994.

(32) Carter-Fenk, K.; Lao, K. U.; Liu, K.-Y.; Herbert, J. M. Accurate and Efficient Ab Initio Calculations for Supramolecular Complexes: Symmetry-Adapted Perturbation Theory with Many-Body Dispersion. *J. Phys. Chem. Lett.* **2019**, *10* (11), 2706–2714.

(33) Herbert, J. M.; Jacobson, L. D.; Lao, K. U.; Rohrdanz, M. A. Rapid Computation of Intermolecular Interactions in Molecular and Ionic Clusters: Self-Consistent Polarization plus Symmetry-Adapted Perturbation Theory. *Phys. Chem. Chem. Phys.* **2012**, *14* (21), 7679–7699.

(34) Peppas, N.; Huang, Y.; Torres-Lugo, M.; Ward, J. H.; Zhang, J. Physicochemical Foundations and Structural Design of Hydrogels in Medicine and Biology. *Annu. Rev. Biomed. Eng.* **2000**, *2*, 9–29.

(35) Eelkema, R.; Pich, A. Pros and Cons: Supramolecular or Macromolecular: What Is Best for Functional Hydrogels with Advanced Properties? *Adv. Mater.* **2020**, *32* (20), e1906012.

(36) Kharkar, P. M.; Kiick, K. L.; Kloxin, A. M. Designing Degradable Hydrogels for Orthogonal Control of Cell Microenvironments. *Chem. Soc. Rev.* **2013**, *42* (17), 7335–7372.

(37) Alshaikh, R. A.; Waeber, C.; Ryan, K. B. Polymer Based Sustained Drug Delivery to the Ocular Posterior Segment: Barriers and Future Opportunities for the Treatment of Neovascular Pathologies. *Adv. Drug Deliv. Rev.* **2022**, *187* (114342), 114342.

(38) Yan, C.; Pochan, D. J. Rheological Properties of Peptide-Based Hydrogels for Biomedical and Other Applications. *Chem. Soc. Rev.* **2010**, *39* (9), 3528–3540.

(39) Tsang, M. Y.; Tokuda, S.; Han, P.-C.; Wang, Z.; Legrand, A.; Kawano, M.; Tsujimoto, M.; Ikeno, Y.; Urayama, K.; Wu, K. C.-W.; Furukawa, S. Controlled Sequential Assembly of Metal–Organic Polyhedra into Colloidal Gels with High Chemical Complexity. *Small Struct.* **2022**, *3* (8), 2100197.

(40) Wang, Z.; Ozcan, A.; Craig, G. A.; Haase, F.; Aoyama, T.; Poloneeva, D.; Horio, K.; Higuchi, M.; Yao, M.-S.; Doherty, C. M.; Maurin, G.; Urayama, K.; Bavykina, A.; Horike, S.; Gascon, J.; Semino, R.; Furukawa, S. Pore-Networked Gels: Permanently Porous Ionic Liquid Gels with Linked Metal-Organic Polyhedra Networks. *J. Am. Chem. Soc.* **2023**, *145* (26), 14456–14465.

(41) Burke, D. W.; Yamashita, M.; Wang, Z.; Kuzumoto, M.; Urayama, K.; Saito, K.; Furukawa, S. Mechanically Tunable Porous Gels Constructed via the Dual Co-Ordination/Covalent Polymerization of Coumarin-Functionalized Rhodium-Organic Cuboctahedra. *Chem. Sci.* **2025**. https://doi.org/10.1039/d5sc00535c.

(42) Wang, Z.; Aoyama, T.; Sánchez-González, E.; Inose, T.; Urayama, K.; Furukawa, S. Control of Extrinsic Porosities in Linked Metal-Organic Polyhedra Gels by Imparting Coordination-Driven Self-Assembly with Electrostatic Repulsion. *ACS Appl. Mater. Interfaces* **2022**, *14* (20), 23660–23668.

(43) Troyano, J.; Tayier, F.; Phattharaphuti, P.; Aoyama, T.; Urayama, K.; Furukawa, S. Porous Supramolecular Gels Produced by Reversible Self-Gelation of Ruthenium-Based Metal-Organic Polyhedra. *Chem. Sci.* **2023**, *14* (35), 9543–9552.

(44) He, L.; Hsu, H.-K.; Li, L.; Lin, L.-T.; Tu, T.-H.; Ong, T.-G.; Liou, G.-G.; Chan, Y.-T. A 10-Nm-Sized Multicompartment Cuboctahedron and Its 2D Hierarchical Arrays Observed by Cryo-EM. *Chem* **2022**, *8* (2), 494–507.

(45) Osterrieth, J. W. M.; Rampersad, J.; Madden, D.; Rampal, N.; Skoric, L.; Connolly, B.; Allendorf, M. D.; Stavila, V.; Snider, J. L.; Ameloot, R.; Marreiros, J.; Ania, C.; Azevedo, D.; Vilarrasa-Garcia, E.; Santos, B. F.; Bu, X.-H.; Chang, Z.; Bunzen, H.; Champness, N. R.; Griffin, S. L.; Chen, B.; Lin, R.-B.; Coasne, B.; Cohen, S.; Moreton, J. C.; Colón, Y. J.; Chen, L.; Clowes, R.; Coudert, F.-X.; Cui, Y.; Hou, B.; D'Alessandro, D. M.; Doheny, P. W.; Dincă, M.; Sun, C.; Doonan, C.; Huxley, M. T.; Evans, J. D.; Falcaro, P.; Ricco, R.; Farha, O.; Idrees, K. B.; Islamoglu, T.; Feng, P.; Yang, H.; Forgan, R. S.; Bara, D.; Furukawa, S.; Sanchez, E.; Gascon, J.; Telalović, S.; Ghosh, S. K.; Mukherjee, S.; Hill, M. R.; Sadiq, M. M.; Horcajada, P.; Salcedo-Abraira, P.; Kaneko, K.; Kukobat, R.; Kenvin, J.; Keskin, S.; Kitagawa, S.; Otake, K.-I.; Lively, R. P.; DeWitt, S. J. A.; Llewellyn, P.; Lotsch, B. V.; Emmerling, S. T.; Pütz, A. M.; Martí-Gastaldo, C.; Padial, N. M.; García-Martínez, J.; Linares, N.; Maspoch, D.; Suárez Del Pino, J. A.; Moghadam, P.; Oktavian, R.; Morris, R. E.; Wheatley, P. S.; Navarro, J.; Petit, C.; Danaci, D.; Rosseinsky, M. J.; Katsoulidis, A. P.; Schröder, M.; Han, X.; Yang, S.; Serre, C.; Mouchaham, G.; Sholl, D. S.; Thyagarajan, R.; Siderius, D.; Snurr, R. Q.; Goncalves, R. B.; Telfer, S.; Lee, S. J.; Ting, V. P.; Rowlandson, J. L.; Uemura, T.; Iiyuka, T.; van der Veen, M. A.; Rega, D.; Van Speybroeck, V.; Rogge, S. M. J.; Lamaire, A.; Walton, K. S.; Bingel, L. W.; Wuttke, S.; Andreo, J.; Yaghi, O.; Zhang, B.; Yavuz, C. T.; Nguyen, T. S.; Zamora, F.; Montoro, C.; Zhou, H.; Kirchon, A.; Fairen-Jimenez, D. How Reproducible Are Surface Areas Calculated from the BET Equation? *Adv. Mater.* **2022**, *34* (27), e2201502.

(46) Larrañeta, E.; Lutton, R. E. M.; Woolfson, A. D.; Donnelly, R. F. Microneedle Arrays as Transdermal and Intradermal Drug Delivery Systems: Materials Science, Manufacture and Commercial Development. *Mater. Sci. Eng. R Rep.* **2016**, *104*, 1–32.

TOC Graphic